

Published in final edited form as:

J Biomol Struct Dyn. 2012 ; 29(5): 985–998. doi:10.1080/073911012010525027.

Permeation Pathway of Homomeric Connexin 26 and Connexin 30 Channels Investigated by Molecular Dynamics

Francesco Zonta^{1,2}, Guido Polles³, Giuseppe Zanotti^{3,4}, and Fabio Mammano^{1,2,3,5,*}

¹Department of Physics and Astronomy "G.Galilei", University of Padua, 35129 Padua, Italy

²Consorzio Nazionale Universitario per le Scienze Fisiche della Materia (CNISM), 35129 Padua, Italy

³Venetian Institute of Molecular Medicine, Foundation for Advanced Biomedical Research, 35129 Padua, Italy

⁴Department of Biological Chemistry, University of Padua, 35129 Padua, Italy

⁵CNR Institute of Neurosciences, Padua Section, 35121 Padua, Italy

Abstract

Mutations in the genes GJB2 and GJB6 encoding human connexin26 (hCx26) and connexin30 (hCx30), respectively, are the leading cause of non-syndromic prelingual deafness in several human populations. In this work, we exploited the high degree (77%) of sequence similarity shared by hCx26 and hCx30 to create atomistic models of homomeric hCx26 and hCx30 connexons starting from the X-ray crystallographic structure of an intercellular channel formed by hCx26 protomers at 3.5-Å resolution. The equilibrium dynamics of the two protein complexes was followed for 40 ns each by Molecular Dynamics (MD) simulations. Our results indicate that, in hCx26, positively charged Lys41 residues establish a potential barrier within the fully open channel, hindering ion diffusion in the absence of an electrochemical gradient. A similar role is played, in hCx30, by negatively charged Glu49 residues. The different position and charge of these two ion sieves account for the differences in unitary conductance observed experimentally. Our results are discussed in terms of present models of voltage gating in connexin channels.

Introduction

Connexins (Cx) are tetraspan transmembrane proteins that form hexameric assemblies in the plasma membrane known as hemichannels or connexons (1-3). The four transmembrane (TM) helices (TM1-TM4) in a connexin protein are connected by two extracellular (EC) loops (EC1, EC2) and a cytoplasmatic loop (CL). Head-to-head docking of two connexons in adjacent cells establishes intercellular channels that cluster into a plaque, and the two adjoining plasma membranes in the plaque remain separated by a narrow extracellular gap of 2-3 nm (4, 5). The wide aqueous pores of connexons are permeable to a variety of cytoplasmic molecules, including virtually all soluble second messengers, amino acids, nucleotides, calcium ions, glucose and its metabolites, and this property underlies the widespread interest in the biological functions of connexin channels (6, 7). There is also considerable interest for channel dysfunction, as connexin mutations have been linked to

© Adenine Press (2012)

*Corresponding author: Fabio Mammano, Phone/Fax: +39 049 7923 231/266, fabio.mammano@unipd.it.

Conflict of Interest

The authors declare no competing commercial interests in relation to the submitted work.

several human diseases such as X-linked Charcot-Marie-Tooth syndrome (CMTX, a peripheral neuropathy), skin diseases, cataracts, oculodentodigital or oculodentosseous dysplasia and deafness (8, 9).

GJB2, the gene encoding human connexin26 (hCx26), was the first gene to be linked to an autosomal recessive form of deafness, DFNB1 (10), as well as to a rare dominant form of deafness, DFNA3 (11). More than 90 distinct recessive mutations of GJB2 have been described, including nonsense, missense, splicing, frame-shift mutations and inframe deletions (12) (see also <http://davinci.crg.es/deafness/index.php>). Altogether these mutations account for approximately 50% of congenital, recessively inherited, sensorineural nonsyndromic hearing loss in several populations, with approximate carrier frequency of 1 in 33 and up to 1 in 28 amongst Mediterraneans (13) (see also <http://hereditaryhearingloss.org/>). DFNB1-linked familial cases with no mutation in GJB2 have also been reported and shown to be associated with two large deletions occurring upstream of GJB2 in GJB6, the gene encoding human connexin30 (hCx30) which lies 30 kb telomeric to GJB2 on chromosome 13 (chromosome 14 in the mouse) (12). To date, a threonine-to-methionine substitution at position 5 is the only hCx30 mutation (hCx30T5M) associated to DFNA3 (14).

Cx26 and Cx30 exhibit the highest degree of amino acid sequence similarity (77%) within the family of connexin proteins (Figure 1). Both are highly expressed in non-sensory cells of the inner ear where they form intercellular gap junction networks that interconnect virtually all non-sensory cells of the sensory epithelium that lines the cochlear duct (15, 16). The recently published X-ray crystallographic structure of a homomeric intercellular channel formed by hCx26 protomers at 3.5-Å resolution is the only connexin crystal structure available to date (17) (Protein Data Bank accession code 2ZW3). It overcomes several limitations of previous work (18-21) and opens unprecedented opportunities for the study of the function of these proteins, including the possibility of using MD to investigate the relationships between channel structure and function (22-24).

Here we report the construction of MD models for hCx26 and hCx30 connexons embedded in a realistic environment comprising plasma membrane phospholipids, explicit solvent (water molecules) and a sufficient number of ions to simulate normal ionic strength (Figure 2). Each model system comprised over 2×10^5 atoms, with initial alpha-carbon (C^α) positions derived from the 3.5-Å X-ray crystallographic structure of hCx26 (17). Our MD simulations focused on permeation properties of the hCx26 and hCx30 connexons, as well as on general features such as structural stability. Our results indicate that residues at TM1/EC1 boundary and in the extracellular cavity are critical for the permeation of charged species. Furthermore, we show that EC1 and EC2 form relatively stiff domains that do not depart significantly from the crystal structure in the simulation time window, despite the lack of a second docked connexon. These data are discussed in terms of present models of voltage gating in connexin channels.

Results

Main Structural and Dynamic Characteristics of the Two MD Models

After performing an initial energy minimization, we followed system dynamics for 40 ns using the approach detailed in the Materials and Methods. To ensure that both MD connexon models achieved a stable steady state, we analyzed root mean square deviations (RMSD) from the initial configurations (Figure 3) for TM (black traces) and EC domains (grey traces), respectively. After 15 ns, the RMSD remained substantially invariant for both structures, indicating that the models had equilibrated in this relatively short time span. Comparison of the hCx26 X-ray model (Figure 4A-C, blue) and our hCx26 MD model

(Figure 4A-C, red) shows an average deviation of 2.0 Å, well within the resolution limit of the experimental data. Similar results also apply to hCx30 (Figure 4D-F, orange). Of notice, the extracellular loops of hCx30 are similar to those of hCx26 (Figure 4C, F), and both maintained the tertiary structure of the Crystal despite the lack of a second docked connexon in our simulations. The RMSDs for the hCx30 MD connexon model are about 0.5 Å lower than those of the hCx26 MD model (Figure 3) because the hCx30 structure was derived from that of hCx26 after rearrangements, due to atom clashes and insertion into the phospholipid bilayer, had yielded a partially relaxed configuration. All the analyses reported in the rest of this article were performed using connexon configurations in the equilibrated regime, namely after the first 15 ns of MD, for both models.

To gain insight into the mobility of connexin domains, we studied fluctuations around the mean values of atomic positions (RMSF, see Materials and Methods for a precise definition) after the attainment of equilibrium. RMSF indicates of how much an atom oscillates around its mean position; they were computed for the C^a of each connexin and averaged over the six subunits (Figure 5, top). In addition, we computed force constants, *i.e.* rigidity profile, which represent how much an atom is bound to all other atoms in the whole connexons (Figure 5, bottom). Peaks in the rigidity profiles intercalate with minima of the fluctuation functions, with the exception of the N-terminal region (NT), indicating that NT fluctuations occur in a coordinated fashion with the rest of the connexon.

These results show that, overall, the dynamic behavior of the two MD models was very similar. In particular, the most stable protomer domains were located in TM1 and TM2. Within the EC domain, EC1 was remarkably stable, despite the lack of the second docked connexon in these simulations; this rather surprising result can be ascribed to the short 3₁₀ helix present in EC1, the beta sheet between EC1 and EC2 and three disulphide bridges between the six cysteine residues, altogether contributing to the rigidity of the tertiary structure. The CL in both models was very mobile (not shown for clarity), consistent with the absence of the CL from hCx26 crystal structure. Finally, the NT domain displayed an intermediate degree of flexibility in both models.

The Permeation Pathway

The permeation pathway of the two connexons is formed by a positively charged cytoplasmic channel entrance, a pore funnel followed by globally negatively charged path and extracellular cavity (Figure 6A, C). The cytoplasmic entrance is formed by the intracellular segments of TM2 and TM3 (Figure 6B, D), with nine and two positively charged residues, respectively. As predicted by earlier studies (25-27), the pore funnel is formed by the NT of the six connexin protomers, which fold back into the vestibule and comprise amino acids 1 to 12, of which residues 5 to 11 are arranged in a helical conformation, denoted as NTH (17). The NT of hCx26 differs from that of hCx30 by two sole amino acids: Gln in position 7 and Ile in position 9 of hCx26 are replaced respectively by His and Phe in hCx30. TM1 and TM2 face the luminal side of the pore, however TM1 is the main helix lining the pore in the plasma membrane region. TM1 is also the most rigid domain of the connexon (Figure 5, bottom), consistent with a structural backbone role. TM3 and TM4 are on the perimeter of the hemichannel facing the lipid environment. This finding contrasts with modeling studies on channels formed by Cx32 based on lower resolution structures, modeling, and evolutionary inferences, which suggested TM3 was the primary pore-lining helix (28, 29). Pore lining residues that protrude most into the pore are highlighted in (Figure 6B, D).

Pore Properties

In the hCx26 X-ray model, the NTH dock to the TM1 helix of the neighboring connexin, and it has been suggested that the NTs are stabilized by a circular girdle of hydrogen bonds between Asp2 and Thr5, supported by the hydrophobic interactions between Trp3 (at the start of the NTH) and the side chain of Met34 in TM1 (17, 30) (Figure 7A). Hydrogen bonds between Asp2 and Thr5 were not reproduced in the MD models; furthermore, hydrophobic interactions buried Trp3 deeper between TM2 of the same protomer and TM1 of the adjacent connexin (Figure 7B, C).

Altogether, these differences in the pattern of interactions resulted in a different positioning of the NTHs and wider pore funnels in the MD models compared to the X-ray model. We used the HOLE software (31) to evaluate pore diameter, taking into account van der Waals interactions, as a function of the coordinate along the six-fold axis. In all three models, relative minima in the pore diameter were found in the funnel region, at the level of Asp2, as well as at the top of the extracellular cavity, at the level of Leu56 (Figure 6B, D). The Asp2 minimum is an absolute one for the pore of the X-ray model (0.97 nm), but not for the hCx26 (1.20 ± 0.15 nm) and hCx30 MD models (1.29 ± 0.13 nm) (Figure 7). In the X-ray model, Lys 41 at the TM1/EC1 border corresponds to a relative minimum of the pore width, with a diameter of about 1.3 nm, whereas in the hCx26 MD model it creates the narrowest constriction, with a diameter of 1.04 ± 0.10 nm. The positively charged Lys41 and the neutral Ala49 of hCx26 are respectively replaced by neutral Gln41 and negatively charged Glu49 in the hCx30 MD model (Figure 6B, D). Glu49, located past the β_{10} helix in the extracellular cavity, creates the narrowest constriction in the hCx30 MD model, with a diameter of 0.94 ± 0.07 nm.

Free Motion of Monoatomic Ions Along the Pore

The free motion of monoatomic ions provides important insight on key residues affecting pore permeation properties. Trajectories of potassium and chloride ions were generated in the course of our equilibrium dynamics, in the absence of an external electrical field (Figure 8). As expected from electrostatics (Figure 6A, C), ions accumulated in the proximity of the cytoplasmic entrance and within the extracellular cavity (Figure 9). Ion transits through the pore were hampered by the charged rings at the level of the Lys41 constriction in the hCx26 MD model and the Glu49 constriction in the hCx26 MD model. Indeed, no ion traversed the hCx26 MD model during the 40 ns dynamics due to the potential barrier generated by Lys41; a single chloride ion trespassed the Glu49 ring in the hCx30 MD model. The potential barriers are mainly electrostatic as (i) water molecules diffused freely along both channel pores and (ii) Gln41 in hCx30 and Ala49 in hCx26 did not hamper the motion of chloride and potassium ions. Chloride ions were driven past the Lys41 barrier of the hCx26 MD model in simulations that included an electrical potential, mimicking a cell membrane potential V_m of -80 mV, which is commonly used in experimental studies on these channels; see *e.g.* ref. (32). Altogether these results indicated that our MD models represent ion permeating channels, in accord with the suggestion that the crystal structure of the hCx26 channel is in an open conformation (17, 30). It remains to be established where the latter describes a channel in the fully open state or in a subconductance state.

Work Required for Ion Permeation

To gain further insight into the role played by pore constrictions in shaping the permeation pathways of hCx26 and hCx30 connexons, we forced the passage of a potassium ion through the pore at a constant (mean) velocity of 0.5 nm/ns using steered molecular dynamics (SMD, see Materials and Methods) (54) and computed the work done in this process (Figure 10). Of notice, the work profile for hCx30 (Figure 10, solid line) presents a single well, corresponding to the position of Glu49. By contrast, the profile for hCx26 (Figure 10, dash-

dot line) exhibits two wells separated by a peak due to the embedding of the positively charged Lys41 constriction within a negatively charged pathway (Figure 6A, B). Thus, despite the high level of sequence similarities of hCx26 and hCx30 (Figure 1), the different locations and charges of these two constrictions generate remarkably different energy landscapes, strengthening the conclusion that these are the two most important residues involved in permeation of charged moieties.

Calcium Binding and Loop Gating

A vast body of single channel recording data, support the notion that connexin channels exhibit two distinct voltage gating processes. The first, termed “ V_j gating” is dependent on the difference in the potential of two coupled cells; the second, termed “loop” or “slow gating”, is inherent to all functional hemichannels and accounts for the voltage-gated opening of unopposed hemichannels upon the depolarization of the membrane potential, V_m (34). Moreover, it is well known that loop gating depends critically on the extracellular Ca^{2+} concentration ($[\text{Ca}^{2+}]_o$) (20, 35, 36). Ground-breaking work performed on the closely related Cx32 hemichannels has concluded that (i) Ca^{2+} can block both voltage gated opening to the higher conductance open state and ion conduction through the partially open hemichannels and (ii) the effect depends on Ca^{2+} binding sites, with millimolar affinity, within the extracellular vestibule of the pore (37).

To explore the issue of loop gating in the context of our hCx26 MD model, we introduced four Ca^{2+} ions into the extracellular vestibule of the pore and followed their dynamics for three different values of the simulated membrane potential V_m . At $V_m = -80$ mV, our simulations show Ca^{2+} ions interacted with residues Glu42, Asp46, Glu47 and Glu50, and remained in their proximity (Figure 11A, left), consistent with the hypothesis that the binding of several Ca^{2+} ions near the point of narrowest pore constriction (Lys41) could cause the physical occlusion of the pore lumen, thereby compromising the inward flow of ions at negative voltages (37). At $V_m = 0$ mV (Figure 11A, right), the interactions weakened and the mean z position of the Ca^{2+} ions shifted significantly towards the extracellular space ($P < 10^{-16}$, U test; Figure 11B). Interactions were completely broken at $V_m = +80$ mV, and Ca^{2+} ions escaped from the vestibule.

Discussion

Both from a structural and from a dynamic point of view, our simulations indicate that the two MD connexon models are very similar and display comparable rigidity profiles and atomic fluctuations around the equilibrium. Comparison of the MD models with the X-ray model shows overall agreement, at the atomic position level, within the resolution of the experimental data. However, pore diameter has an absolute minimum at the Asp2 level in the NT of the hCx26 X-ray model, with its proposed circular girdle of hydrogen bonds between Asp2 and Thr5, but not in the hCx26 and hCx30 MD models, in which hydrogen bonds between Asp2 and Thr5 were not formed. The 2 Å wider diameters in the MD models associate with different positioning of the NT compared to the X-ray model, and could be explained by considering that (i) the channels in the 3D crystals were not surrounded by the plasma membrane and (ii) a dehydration process was used to improve the resolution of the crystal reconstruction (17). Rigidity profiles for the two MD connexon models featured prominent peaks around Met34. The highly conserved Trp3 is reported to undergo a hydrophobic interaction with Met34 from the neighboring monomer in the Cx26 X-ray model, and the interaction is proposed to draw the pore funnel onto the innermost wall of the channel, keeping it in the open state (17, 30). Met34 is conserved in Cx26, Cx30, Cx32, Cx40, Cx40.1, Cx59 and Cx62, and our MD simulations indicate that Met34 and Trp3 mediate the same hydrophobic interaction also in the hCx26 and hCx30 MD models.

The most relevant differences between the permeation pathways of the two MD models are related to two crucial pore lining residues, 41 and 49, that are not conserved in the two proteins. The presence of charged residues protruding into the pore lumen creates electrostatic barriers that regulate the transit of charged species. Indeed, our results indicate that Lys41 in hCx26 and Glu49 in hCx30 shape the energy landscape of their respective pores; they are also the main determinants of unitary conductance, as the size of the two pores are nearly identical. We can derive a simple estimate (zero order approximation) for the unitary conductance ratio of hCx26 vs. hCx30 connexons based on the following rationale. The probabilities of escaping from a potential well of depth W (in Joule, J) is proportional to the Boltzmann factor $e^{-W/k_B T}$, T is absolute temperature (in Kelvin, K) and k_B is the Boltzmann constant ($1.38 \times 10^{-23} \text{ J K}^{-1}$). Our simulations delineate a single potential well along the pore axis for hCx30, with depth $W_0/k_B T = 7.210$. By contrast, the positively charged Lys41 residue within a negatively charged environment in hCx26 delineates a double potential well with depths $W_1/k_B T = 2.93$ and $W_2/k_B T = 4.83$ (Figure 10). As flux is an exponential function of potential (38), the unitary conductance, σ_{CX30} , of the hCx30 connexon can be assumed to be proportional to the Boltzmann factor of its single well, that is $\sigma_{CX30} = \alpha e^{-W_0/k_B T}$. Instead, since the probabilities of escaping from each of the two wells in hCx26 are independent, the analogous quantity $\sigma_{CX26} = \alpha e^{-W_1/k_B T} e^{-W_2/k_B T}$. Thus, based on our MD simulations, we conclude that $\sigma_{CX30}/\sigma_{CX26} \approx 1.72$, in fair agreement with the experimentally determined ratio of $160 \text{ pS}/110 \text{ pS} = 1.45$ (39). Of course, more refined considerations may yield a closer match between simulations and experiments. Of notice, hCx31 channels exhibit 2 positively charged residues in this critical region, namely Arg42 and Lys49, and their unitary conductance is about half that of hCx30 channels (40).

Lys41 of hCx26 and Glu49 of hCx30 are found at opposite ends of the extracellular vestibule, which is thought to be critical for the Ca^{2+} dependence of the loop gating process (34). The proposed mechanism, based on pore occlusion by Ca^{2+} ions binding in a voltage-dependent manner with millimolar affinity to acidic residues within the vestibule, is rather attractive for its simplicity and interpretative power (37). A similar co-factor role for Ca^{2+} ions has been described for the gating of sodium channels (41, 42). Indeed, this mechanism is compatible with the results of our simulations as well as with the reported conformational changes in surface profiles of hCx26 connexons (see Figure 3B and Figure 4B of ref. (20)). Furthermore, a loop gating mechanisms involving the progressive and stochastic release of Ca^{2+} from the outer vestibule (to which it appears to be weakly bound) as the potential becomes less hyperpolarized can account for the opening at negative potentials that frequently involves ill-defined transitions between the closed state and a main open state (34).

Based on work performed with a chimera in which the first extracellular loop of Cx32 is replaced by that of Cx43, a different loop gating mechanism has been proposed, which involves the substantial rotation of the TM1 helix (43, 44). The rigidity profiles of hCx26 and hCx30 connexons in the extracellular vestibule are difficult to reconcile with a substantial structural reorganization of this region. Furthermore, Cx43 belongs to the “alpha” connexin family, whereas Cx26, Cx30 and Cx32 are “beta” connexins; members of these two classes are distinguished on the basis of their primary sequence and overall predicted topological organization (45). Thus, the gating mechanisms could well be different for these different connexin families.

As depolarization progresses, hCx26 hemichannels remain stable in a high conductance open state until polarization reaches positive potentials; at this point the single hemichannels close to a subconductance state with rapid transitions (~1-2 ms), which are similar in appearance to the fast gating transitions controlled by transjunctional voltage, V_j , in the

corresponding homotypic intercellular channels (26, 33, 34). By contrast, in other types of connexin hemichannels, *e.g.* those formed by Cx32, the conductance increases monotonically throughout the whole voltage range explored (46). In most connexins, this difference is accounted for by differently charged amino acid residues in the first positions of the NT, and possibly two positions at the TM1/EC1 border (34). Thus, the positive valence of the Cx32 voltage sensor has been attributed to the NH⁺₃ group of Met1, which is the only charge present in the NT up to residue 14 in this connexin, and is thought to be responsible for channel closure at relative negative potentials on the cytoplasmic side. By contrast, other connexins that close at relative positive potentials on the cytoplasmic side, including Cx26 and Cx30, are characterized by a globally neutral or negatively charged NT (34). In Cx26 and Cx30, the negatively charged COO⁻ group of Asp2 and the NH⁺₃ group of Met1 form a dipole with an electric dipole moment of ~1.4×10⁻²⁸ C m, which is 22-fold larger than that of a water molecule (6.2×10⁻³⁰ C m). The Met1-Asp2 dipole is bound to orient and translate in the electric field gradient within the channel pore, and this movement may promote gating transitions when V_j polarity is altered. Consistent with this interpretation, exchange of the negatively charged Asp2 in Cx26 by the uncharged (Asn or Gln) or positive (Arg or Lys) charged residues reverses the polarity of closing from positive to negative; vice versa, replacement of the uncharged Asn2 in Cx32 to a negatively charged residue (Glu or Asp), but not a positively charged amino acid (Arg or Lys) or another uncharged residue (Gln or Ala), reverses the negative polarity to positive (27). The proposed voltage sensor of hCx26 would foster the V_j gating mechanism by movement of the NT (17, 30), which is connected to TM1 by a flexible loop (25). This gating mechanism (i) is consistent with fluctuation analysis of our MD models, indicating that the NT is relatively mobile, (ii) agrees with the high crystallographic temperature of the NT in the hCx26 crystal structure (17) and (iii) applies to both hCx26 and hCx30 connexons. Future studies will continue to unravel, at the atomic level, the intricacies of gating mechanism in connexin channels, and we believe MD will play a major role in the discovery process.

Materials and Methods

MD Modeling of the hCx26 and hCx30 Connexons

The crystal structure of hCx26 presents domains that are flexible or not well defined, namely the first residue (Met1), the CL (residues 110 to 124) and a short segment of the C-terminus (residues 218-226). We added the missing amino acids starting from their C^a, with positions assigned so as to mimic a random loop for both CL and C-terminus. The coordinates of the Met1 C^a were assigned in register with NTH which follows it. All other atoms which were missing from the X-ray model, including hydrogen atoms, were added using the LEAP module of the Amber 9.0 software (47) and Amber03 force field parameters (50). Thereafter a 60 ps *in vacuo* MD run was performed at 50K while keeping X-ray structure C^a frozen, with the aim of achieving an energetically stable configuration by: (i) eliminating the clashes introduced by the addition of hydrogen atoms and (ii) equilibrating the newly added segments. This initial hCx26 connexon configuration was inserted in a hole opened in a pre-relaxed membrane bilayer of phospholipids (palmytol posphatidyl choline, POPC) and all phospholipids in close contact with the protein were removed. The final membrane configuration comprises 493 phospholipids. The positive net charge of the hCx26 connexon was neutralized with 54 chloride ions; additional pairs of potassium and chloride ions were added to mimic a physiological ionic strength. The system was solvated with a total of 39189 water molecules and a brief relaxation run (100 ps) was performed with restrained dynamics on C^a. This allowed the side chains of TM residues and phospholipids to arrange properly, eliminating clashes and filling small residual membrane fissures.

The configuration generated with the procedure described above was taken as the starting point of our MD simulations, which were performed under periodic boundary conditions.

The unitary cell dimensions ($\sim 12 \times 12 \times 11$ nm) approximate the distance between adjacent channels in a gap-junction plaque, as measured by atomic force microscopy (20). The complete system (proteins, membrane, ions and water molecules) comprised 206188 atoms.

The hCx30 MD connexon model was built from the hCx26 model as described hereafter. Starting from configuration of hCx26 chosen after equilibration of the RMSD of TM and EM regions (*i.e.* after 13 ns of dynamics), we mutated the amino acids that differ in the two sequences (Figure 1) using the Swiss PDB viewer (48). The tail of the hCx30 CT is 35 a. a. longer than that of hCx26. To our knowledge, no detailed structural information of the CT domain is available. Therefore we modeled it using standard techniques of tertiary structure prediction (49). Next, we connected the CT to the rest of the protein, and completed the model by fitting six copies of the hCx30 protomer in the relaxed structure of the hCx26 MD connexon model inserted in the membrane. The total number of atoms in the hCx30 system was 233806. Equilibrium MD simulations of both systems were performed with the Amber 9.0 software (47) and Amber03 force field (50). Temperature and pressure were kept constant using Berendsen's thermostat and barostat (51) at 300 K and 1 atm, respectively. Particle Mesh Ewald summation (52) was used for the long-range electrostatic interactions, with a cut off of 1.0 nm for the direct interactions. Simulations of the two systems with unrestrained conditions lasted 40 ns.

RMSD, RMSF and Rigidity Profiles

RMSD provides a measure of deviation from the first frame during the dynamic evolution of the systems. If $X_i(t)$ is the position vector for the i -th atom at time t , we define RMSD at time t as:

$$\text{RMSD}(t) = \frac{\sum \sqrt{(X_i(t) - X_i(0))^2}}{N} \quad [1]$$

RMSF is the deviation from the mean (averaged over time) and measures how much an atom oscillates around its mean position $\langle X_i \rangle$ it is defined as:

$$\text{RMSF}(i) = \left\langle \sqrt{(X_i(t) - \langle X_i \rangle)^2} \right\rangle, \quad [2]$$

where angled brackets indicate time averages. RMSF in Figure 3 were computed as the mean RMSF of the six connexin subunits.

Force constants measure how much an atom position is bound to the position of the other atoms; they are defined as:

$$k_i = \frac{1}{\langle (d_i - \langle d_i \rangle)^2 \rangle}, \quad [3]$$

where the scalar quantity d_i is the average distance of i -th atoms from all other atoms of the system. The plot of k_i vs. i defines a rigidity profile; peaks in these plots often correspond to residues that are in the active or binding site of the protein (53).

SMD and Computation of the Work Profile for Ion Transit through the Pore

To delineate the energy landscape along the pore axis (potential of mean force) of each hemichannel, we used a SMD approach (54) within the Gromacs 4.5 environment (55). A single potassium ion was restrained in the proximity of the pore axis by an harmonic potential, with a constant of $2000 \text{ kJ mol}^{-1} \text{ nm}^{-2}$ in both x and y directions. A harmonic

potential featuring the same constant was applied on the z direction, and its minimum shifted from the cytoplasmic side to the extracellular side of the channel at a constant velocity of 0.5 nm ns $^{-1}$. The simulations spanned a total of 7.5 nm in 15 ns for each system. The force due to this harmonic potential was saved every 200 fs and work profiles $W(z)$ were computed as

$$W(z) = \int_0^z \mathbf{F}(z') \cdot dz', \quad [4]$$

where $\mathbf{F}(z)$ indicates the elastic force averaged over a 100 ps time window while the ion occupies the mean position z along the six-fold symmetry axis. The shifting harmonic potential was large enough to keep the ion position in the proximity of its minimum with a standard deviation of 0.035 nm. As $\mathbf{F}(z)$ balanced effectively all other forces acting on the ion at coordinate z , $W(z)$ is a reliable estimate of the free energy landscape. Simulations were performed under constant volume conditions on the previously described equilibrated systems.

Dynamics of Free Ca²⁺ Ions

Four Ca²⁺ ions, and associated counter-ions, were added to the hCx26 system and placed inside the extracellular vestibule of the pore. We simulated a potential difference between the cytoplasmic and extracellular side within the Gromacs 4.5 environment by adding a constant electric field parallel to the pore axis corresponding to a potential drop V_m over 5 nm, which is the approximate thickness of the lipid membrane in our simulations. We followed the dynamics of the Ca²⁺ ions for 10 ns in each of the following different situations: $V_m = -80$ mV, $V_m = 0$ mV and $V_m = +80$ mV.

Acknowledgments

Supported by MIUR PRIN grant no. 2009CCZSES and Telethon grant GGP09137 to FM, and from a University of Padova grant to FZ (prot. GRIC101108). Computer simulations were performed at the CINECA and CASPUR supercomputer centers.

References

1. Goodenough DA, Paul DL. *Nat Rev Mol Cell Biol*. 2003; 4:285–294. [PubMed: 12671651]
2. Saez JC, Retamal MA, Basilio D, Bukauskas FF, Bennett MV. *Biochimica et Biophysica Acta*. 2005; 1711:215–224. [PubMed: 15955306]
3. Evans WH, De Vuyst E, Leybaert L. *The Biochemical Journal*. 2006; 397:1–14. [PubMed: 16761954]
4. Calera MR, Wang Z, Sanchez-Olea R, Paul DL, Civan MM, Goodenough DA. *Investigative Ophthalmology & Visual Science*. 2009; 50:2185–2193. [PubMed: 19168903]
5. Maeda S, Tsukihara T. *Cellular and Molecular Life Sciences: CMLS*. 2011; 68:1115–1129. [PubMed: 20960023]
6. Harris AL. *Q Rev Biophys*. 2001; 34:325–472. [PubMed: 11838236]
7. Harris AL. *Prog Biophys Mol Biol*. 2007; 94:120–143. [PubMed: 17470375]
8. Gerido DA, White TW. *Biochimica et Biophysica Acta*. 2004; 1662:159–170. [PubMed: 15033586]
9. Laird DW. *The Biochemical Journal*. 2006; 394:527–543. [PubMed: 16492141]
10. Kelsell DP, Dunlop J, Stevens HP, Lench NJ, Liang JN, Parry G, Mueller RF, Leigh IM. *Nature*. 1997; 387:80–83. [PubMed: 9139825]
11. Denoyelle F, Lina-Granade G, Plauchu H, Bruzzone R, Chaib H, Levi-Acobas F, Weil D, Petit C. *Nature*. 1998; 393:319–320. [PubMed: 9620796]
12. Hilgert N, Smith RJ, Van Camp G. *Curr Mol Med*. 2009; 9:546–564. [PubMed: 19601806]

13. Gasparini P, Estivill X, Volpini V, Totaro A, Castellvi-Bel S, Govea N, Mila M, Della Monica M, Ventruito V, De Benedetto M, Stanziale P, Zelante L, Mansfield ES, Sandkuijl L, Surrey S, Fortina P. *Eur J Hum Genet*. 1997; 5:83–88. [PubMed: 9195157]
14. Grifa A, Wagner CA, D'Ambrosio L, Melchionda S, Bernardi F, Lopez-Bigas N, Rabionet R, Arbones M, Monica MD, Estivill X, Zelante L, Lang F, Gasparini P. *Nature Genetics*. 1999; 23:16–18. [PubMed: 10471490]
15. Martinez AD, Acuna R, Figueroa V, Maripillan J, Nicholson B. *Antioxidants & Redox Signaling*. 2009; 11:309–322. [PubMed: 18837651]
16. Nickel R, Forge A. *Curr Opin Otolaryngol Head Neck Surg*. 2008; 16:452–457. [PubMed: 18797288]
17. Maeda S, Nakagawa S, Suga M, Yamashita E, Oshima A, Fujiyoshi Y, Tsukihara T. *Nature*. 2009; 458:597–602. [PubMed: 19340074]
18. Makowski, L. *Gap Junction*. Bennett, MVL., et al., editors. Cold Spring Harbor Laboratory; 1985. p. 5–12.
19. Unger VM, Kumar NM, Gilula NB, Yeager M. *Science*. 1999; 283:1176–1180. [PubMed: 10024245]
20. Muller DJ, Hand GM, Engel A, Sosinsky GE. *The EMBO Journal*. 2002; 21:3598–3607. [PubMed: 12110573]
21. Oshima A, Tani K, Hiroaki Y, Fujiyoshi Y, Sosinsky GE. *Proceedings of the National Academy of Sciences of the United States of America*. 2007; 104:10034–10039. [PubMed: 17551008]
22. Lindahl E, Sansom MS. *Curr Opin Struct Biol*. 2008; 18:425–431. [PubMed: 18406600]
23. Khalili-Araghi F, Gumbart J, Wen PC, Sotomayor M, Tajkhorshid E, Schulten K. *Curr Opin Struct Biol*. 2009; 19:128–137. [PubMed: 19345092]
24. Wang Y, Shaikh SA, Tajkhorshid E. *Physiology (Bethesda)*. 2010; 25:142–154. [PubMed: 20551228]
25. Purnick PE, Benjamin DC, Verselis VK, Bargiello TA, Dowd TL. *Arch Biochem Biophys*. 2000; 381:181–190. [PubMed: 11032405]
26. Oh S, Rubin JB, Bennett MV, Verselis VK, Bargiello TA. *The Journal of General Physiology*. 1999; 114:339–364. [PubMed: 10469726]
27. Verselis VK, Ginter CS, Bargiello TA. *Nature*. 1994; 368:348–351. [PubMed: 8127371]
28. Fleishman SJ, Unger VM, Yeager M, Ben-Tal N. *Mol Cell*. 2004; 15:879–888. [PubMed: 15383278]
29. Pantano S, Zonta F, Mammano F. *PloS One*. 2008; 3:e2614. [PubMed: 18648547]
30. Maeda E, Ye S, Wang W, Bader DL, Knight MM, Lee DA. *Biomechanics and Modeling in Mechanobiology*. 2011
31. Smart OS, Goodfellow JM, Wallace BA. *Biophysical Journal*. 1993; 65:2455–2460. [PubMed: 7508762]
32. Gonzalez D, Gomez-Hernandez JM, Barrio LC. *Faseb J*. 2006; 20:2329–2338. [PubMed: 17077310]
33. Bukauskas FF, Verselis VK. *Biochimica et Biophysica Acta*. 2004; 1662:42–60. [PubMed: 15033578]
34. Gonzalez D, Gomez-Hernandez JM, Barrio LC. *Prog Biophys Mol Biol*. 2007; 94:66–106. [PubMed: 17470374]
35. Ebihara L, Steiner E. *The Journal of General Physiology*. 1993; 102:59–74. [PubMed: 7690837]
36. Pfahnl A, Dahl G. *Pflugers Archiv: European Journal of Physiology*. 1999; 437:345–353. [PubMed: 9914390]
37. Gomez-Hernandez JM, de Miguel M, Larrosa B, Gonzalez D, Barrio LC. *Proceedings of the National Academy of Sciences of the United States of America*. 2003; 100:16030–16035. [PubMed: 14663144]
38. Chen D, Lear J, Eisenberg B. *Biophysical Journal*. 1997; 72:97–116. [PubMed: 8994596]
39. Beltramello M, Piazza V, Bukauskas FF, Pozzan T, Mammano F. *Nature Cell Biology*. 2005; 7:63–69.

40. Abrams CK, Freidin MM, Verselis VK, Bargiello TA, Kelsell DP, Richard G, Bennett MV, Bukauskas FF. Proceedings of the National Academy of Sciences of the United States of America. 2006; 103:5213–5218. [PubMed: 16549784]
41. Armstrong CM, Cota G. Proceedings of the National Academy of Sciences of the United States of America. 1991; 88:6528–6531. [PubMed: 1650473]
42. Arhem P, Elinder F. Quarterly Reviews of Biophysics. 2003; 36:373–427. [PubMed: 15267168]
43. Tang Q, Dowd TL, Verselis VK, Bargiello TA. The Journal of General Physiology. 2009; 133:555–570. [PubMed: 19468074]
44. Harris AL. The Journal of General Physiology. 2009; 133:549–553. [PubMed: 19468073]
45. Kumar NM, Gilula NB. Semin Cell Biol. 1992; 3:3–16. [PubMed: 1320430]
46. Castro C, Gomez-Hernandez JM, Silander K, Barrio LC. The Journal of Neuroscience: the Official Journal of the Society for Neuroscience. 1999; 19:3752–3760. [PubMed: 10234007]
47. Case DA, Cheatham TE 3rd, Darden T, Gohlke H, Luo R, Merz KM Jr, Onufriev A, Simmerling C, Wang B, Woods RJ. Journal of Computational Chemistry. 2005; 26:1668–1688. [PubMed: 16200636]
48. Guex N, Peitsch MC. Electrophoresis. 1997; 18:2714–2723. [PubMed: 9504803]
49. Roy A, Kucukural A, Zhang Y. Nature Protocols. 2010; 5:725–738.
50. Duan Y, Wu C, Chowdhury S, Lee MC, Xiong G, Zhang W, Yang R, Cieplak P, Luo R, Lee T, Caldwell J, Wang J, Kollman P. Journal of Computational Chemistry. 2003; 24:1999–2012. [PubMed: 14531054]
51. Berendsen HJC, Postma JPM, van Gunsteren WF, Dinola A, Haak JR. The Journal of Chemical Physics. 1984; 81:3684–3690.
52. Darden T, York D, Pedersen L. The Journal of Chemical Physics. 1993; 98:10089–10093.
53. Sacquin-Mora S, Lavery R. Biophysical Journal. 2006; 90:2706–2717. [PubMed: 16428284]
54. Park S, Schulten K. J Chem Phys. 2004; 120:5946–5961. [PubMed: 15267476]
55. Hess B, Kutzner C, van der Spoel D, Lindahl E. Journal of Chemical Theory and Computation. 2008; 4:435–447.

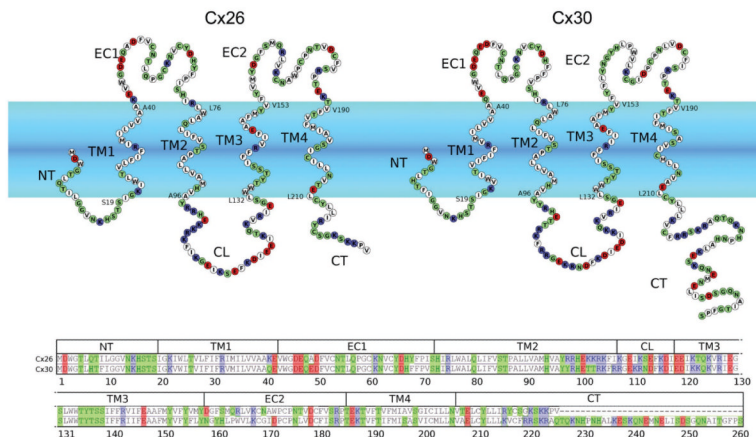


Figure 1.

hCx26 and hCx30 topology representation and sequence alignment. NT, N-terminus; CT, C-terminus; TM1-TM4, transmembrane helices 1 to 4; CL, cytoplasmic loop connecting TM2, TM3; EC1, EC2, extracellular loops connecting TM1 to TM2 and TM3 to TM4, respectively. Residue color code: blue, positive; red, negative; white, hydrophobic; green, hydrophilic.

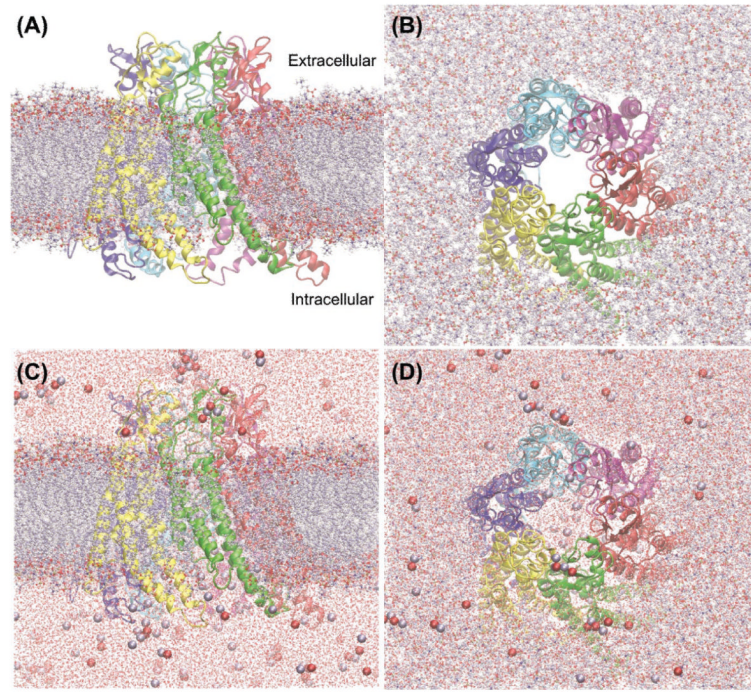


Figure 2.

hCx26 connexon model in a realistic computational environment. (A, B) The connexon is shown embedded in a phospholipid bilayer. (C,D) Also water molecules and ions (shown as colored spheres) were included in the MD simulations, A, C are side views; B, D are views from the extracellular side.

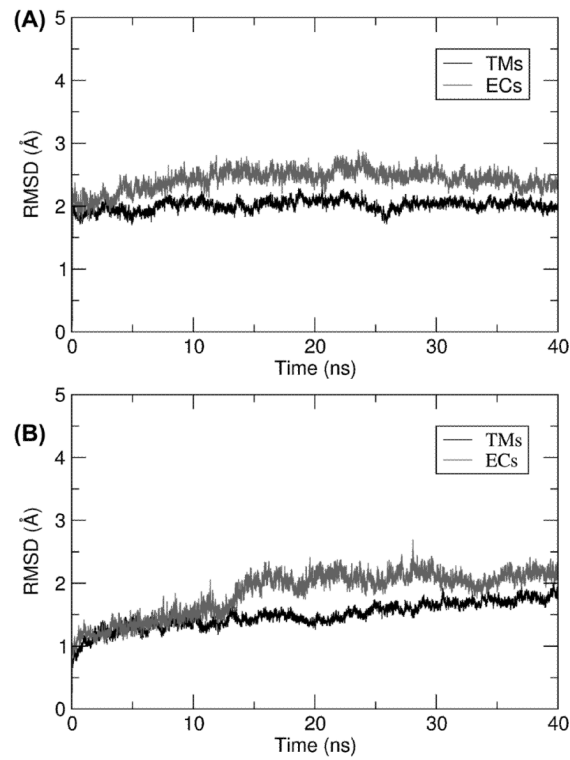
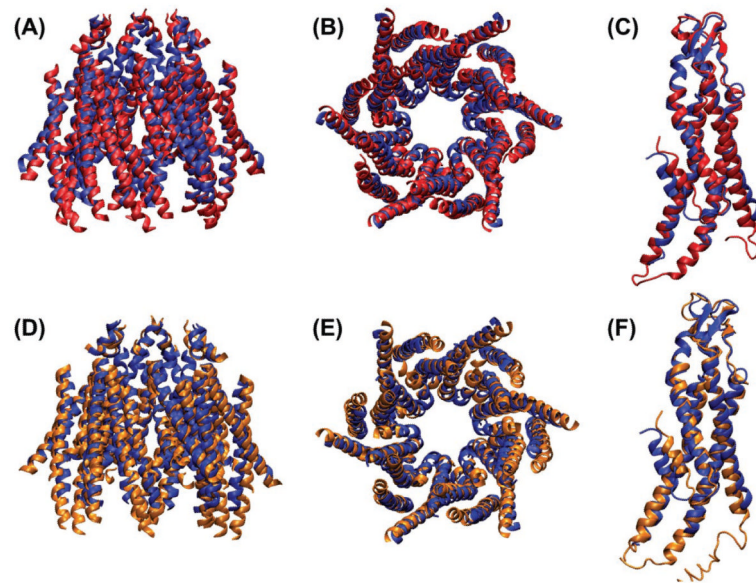


Figure 3.

Plots of RMSD vs. time during the 40 ns of unrestrained dynamics. (A) hCx26. (B) hCx30. Black traces correspond to residues in the membrane region (19 to 40, 76 to 96, 132 to 153 and 190 to 210), whereas grey traces correspond to residues in the extracellular space (41 to 75 and 154 to 189).

**Figure 4.**

Comparison between the hCx26 crystal model and our MD models in cartoon representation. The hCx26 crystal model is shown in blue, the Cx26 MD model in red and the Cx30 MD model in orange. Panels **A**, **B** and **D**, **E** show only the helical regions of the connexons for clarity. Panels **A**, **D** are side views whereas **B**, **E** are views from the cytoplasmic side. Panels **C**, **F** depict single connexins.

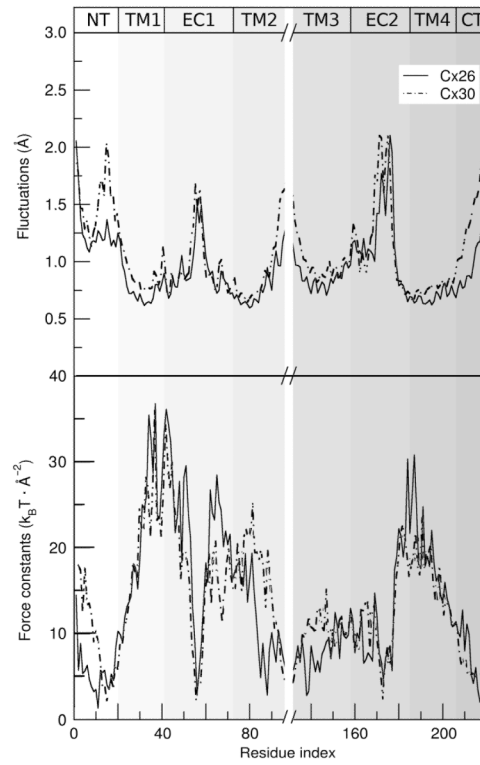
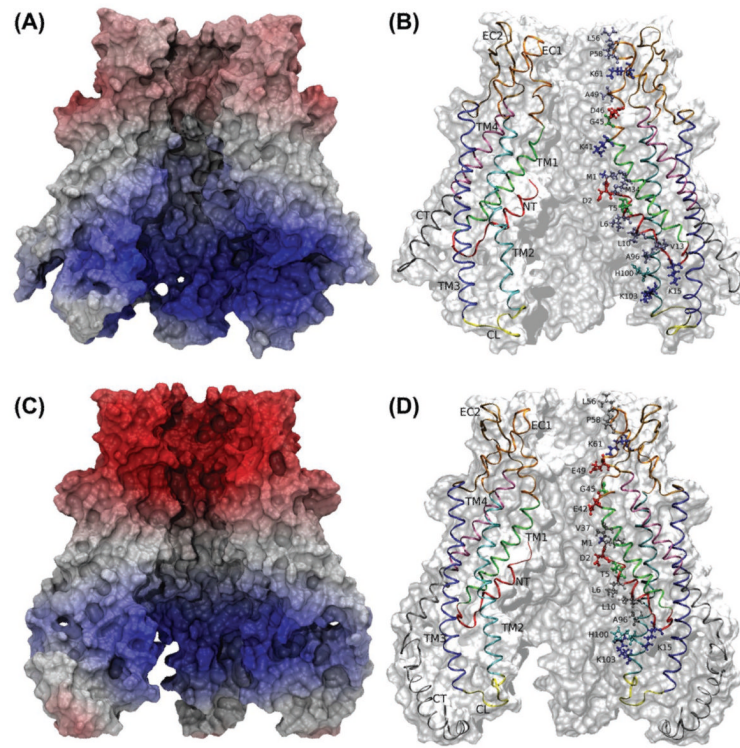


Figure 5.

Fluctuations and force constants of the two MD models vs. residue index. Data pertaining to the (majority of) cytoplasmic domains (residues 97 to 131, and residues from 221 to the C-terminal) are not shown for clarity.

**Figure 6.**

Electrostatics and pore lining residues. **(A, C)** show a representation of the electrostatics, computed from the reciprocal sum of particle mesh Ewald method (with an Ewald factor of 0.25 \AA^{-1}) for hCx26 (**A**) and hCx30 (**C**), projected on the surface of the protein. Negative potential is shown in red, positive in blue. **B, D** depict some of the residues which form the pore wall. The color code for the residues is: red for negatively charged; blue for positively charged; gray for hydrophobic; green for polar. The NT Met1 amino group is charged and thus colored in blue. The whole protein is shown in a ribbon representation and each structural domain is labeled and depicted with a different color.

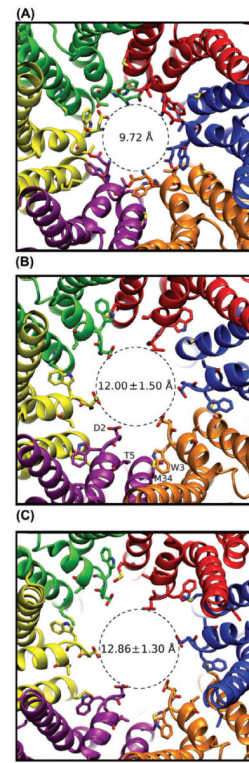


Figure 7.

Cytoplasmic views of the pore funnel generated by the NT domains. (A) Cx26 crystal model. (B) hCx26 MD model. (C) hCx30 MD model. Each connexin subunit is depicted with a different color. Models in panels B and C were generated by averaging atomic positions along the last 25 ns of the MD trajectories, followed by energy minimization.

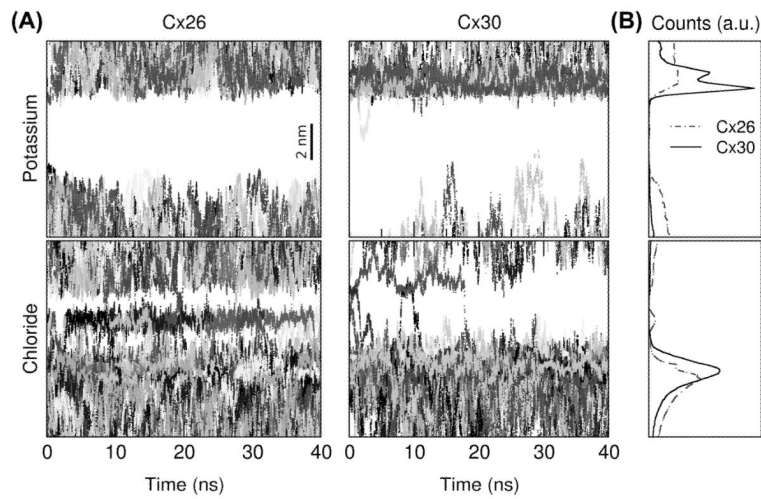
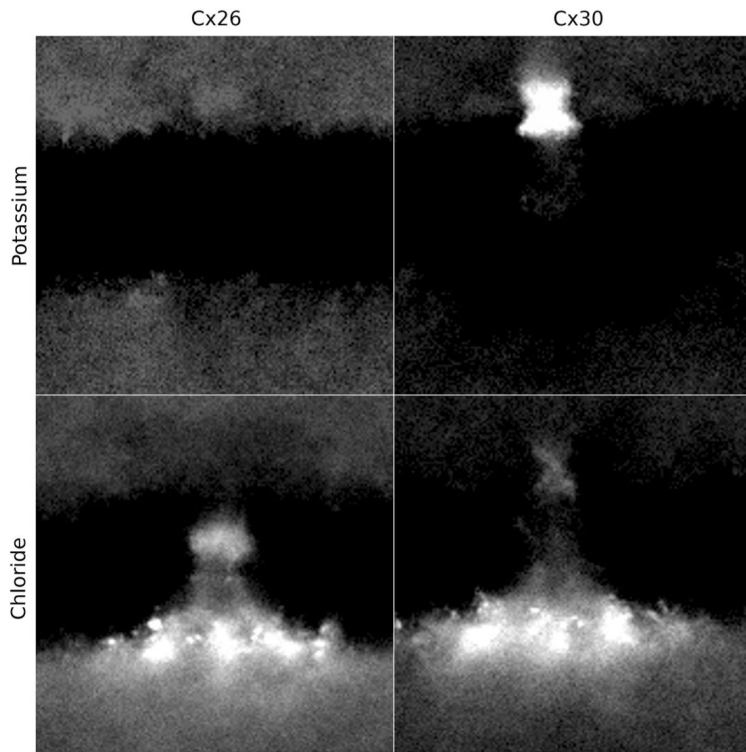


Figure 8.

Free motion of monoatomic ions along the pore. (A) Coordinate along the six-fold symmetry axis vs. time of potassium and chloride ions. (B) Occupancy probability histograms from data in A.

**Figure 9.**

Visualization of ion occupancy probability. Shown are probability density distributions projected on a plane containing the six-fold symmetry axis. Black represents zero, whereas probability values >0 are encoded as increasingly lighter shades of gray.

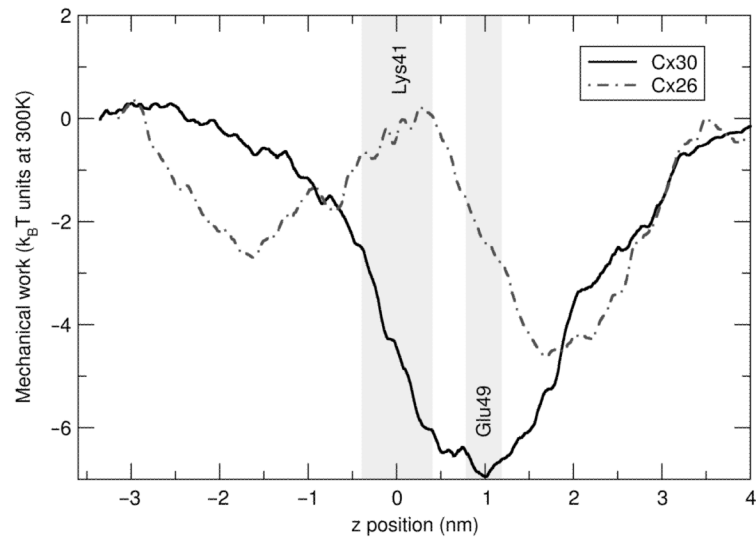
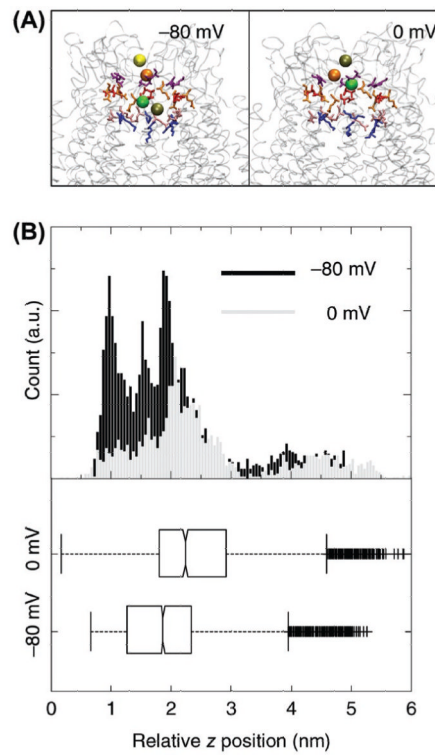


Figure 10.

Work required for permeation of a single potassium ion vs. position along the six-fold symmetry axis. Gray bands indicate the position spanned by the charged groups of Lys41 and Glu49 side chains in the course of the simulations.

**Figure 11.**

Ca^{2+} ion distribution within the pore. (A) Snapshots showing ions positions at $V_m = -80\text{ mV}$ (left) and $V_m = 0\text{ mV}$ (right). Ca^{2+} ions are represented as colored spheres with van der Waals radii; one of the four ions present in the left panel escaped from the vestibule at $V_m = 0\text{ mV}$. Key amino acids are also shown: blue Lys41, pink Glu42, red Asp46, orange Glu47, purple Asp50. (B) Top, occupancy frequency histograms derived from 10 ns of MD. Bottom, box plots from data shown in the top panel.